Transp Porous Med
DOI 10.1007/s11242-015-0529-2

Pore Network Modeling of Drying Processes in Macroporous Materials: Effects of Gravity, Mass Boundary Layer and Pore Microstructure

A. G. Yiotis[1] · **D. Salin**[2] · **Y. C. Yortsos**[3]

Received: 13 January 2015 / Accepted: 10 June 2015

Abstract We develop a pore network model for the evaporative drying of macroporous media that accounts for the major pore-scale mechanisms experimentally identified to play an important role on the drying rates and phase distribution patterns. The model accounts for viscous flow through liquid films, gravity and mass transfer, both within the dry medium and also through a mass boundary layer over the external surface of the medium. Also accounted are the heterogeneity of the pore size distribution and pore wall microstructure effects expressed through the degree of corner roundness. The latter plays a major role on the extent of the film region. The model is then used to study capillary, gravity and external mass transfer effects through the variation of the appropriate dimensionless numbers. The effect of gravity is particularly analyzed for the two cases, when gravity is opposing and when it is enhancing drying, respectively. In the latter case, strong mass transfer and viscous forces compared to gravity can prevent instability of the receding evaporation front, leading to a two constant-rate-regime drying curve in agreement with the 1-D theory proposed earlier.

Keywords Drying · Pore network modeling · Films · Gravity

✉ A. G. Yiotis
yiotis@ipta.demokritos.gr

D. Salin
salin@fast.u-psud.fr

Y. C. Yortsos
yortsos@usc.edu

[1] Environmental Research Laboratory, NCSR Demokritos, 15310 Agia Paraskevi, Greece

[2] FAST Laboratory, University Pierre and Marie Curie, Bâtiment 502, Campus Universitaire d'Orsay, 91405 Orsay Cedex, France

[3] Mork Family Department of Chemical Engineering and Materials Science, Viterbi School of Engineering, University of Southern California, Los Angeles, CA 90089, USA

Published online: 27 June 2015

1 Introduction

Evaporative drying of macroporous materials (i.e., pore sizes greater than 50 nm) is a process encountered in a number of applications of environmental and technological interest. Drying within the complex inner geometry of a disordered medium involves several pore-scale mechanisms that determine the macroscopic dynamics of the process, and specifically the drying rates and the phase distribution patterns (van Brakel 1980; Shaw 1987; Prat 1993). Such processes typically occur in the low-capillary-number regime, and thus the dominant mass transport mechanisms are viscous flow through liquid films that form in the cavities of pore walls, as the liquid–gas interface recedes deeper in the pore space, and diffusion both within and near the external surface of the medium which is open to the environment (Yiotis et al. 2003; Lehmann et al. 2008; Shokri et al. 2008; Faure and Coussot 2010). In addition, buoyancy plays a major role both in the movement of the liquid–gas interfaces, thus on the dynamics of phase distributions (Wilkinson 1984), as well as in film flow, by either opposing or enhancing flow and transport toward the evaporation interfaces (Chauvet et al. 2009; Yiotis et al. 2012a).

The interplay of these mechanisms can be described by three dimensionless numbers: the capillary number, Ca_f, expressing the ratio of viscous over capillary forces at interfaces and in the liquid films; the Bond number, Bo, expressing the ratio of gravity over capillary forces; and the Sherwood number, Sh, describing mass transfer at the external surface of the porous medium. In addition, pore-scale heterogeneity is expressed via the dimensionless standard deviation of the pore-throat size distribution, but also through a spatially uniform parameter, the degree of corner roundness, p, that significantly affects flow through liquid films (Chauvet et al. 2010).

Consider, first, the case when gravity opposes drying, namely when the flow through the films occurs in the direction opposite to the gravity acceleration vector. Under such conditions, drying typically exhibits an early stage, where the evaporation rate is constant, which defines what is known as the constant rate period (CRP) or Stage-1 evaporation. This is followed by a regime characterized by a continuous decrease in the recovery rates, termed falling rate period (FRP) or Stage-2 evaporation (van Brakel 1980). During CRP, the external surface of the porous medium remains wet over extended periods of time, as liquid continuity is maintained through films, despite the fact that connected liquid–gas interfaces (the percolation front) have receded deeper in the medium and do not have macroscopic continuity to the surface. Liquid films that are formed in the cavities of pore walls provide the hydraulic connectivity needed (Shaw 1987; Eijkel et al. 2005). While surface wetness decreases with time due to a combination of phenomena (Yiotis et al. 2003; Lehmann et al. 2008), and as long as liquid films still reach the external surface, the partial pressure of the evaporating species there remains approximately constant, and equal to the vapor pressure of the liquid (This also assumes that the thickness of the external mass transfer layer is significantly larger than the characteristic pore size of the medium (Suzuki and Maeda 1968), which is almost always the case). Thus during the CRP regime, the process is controlled by external mass transfer.

When gravity opposes drying, at a critical film length (or an equivalent critical average distance of the percolation front from the open surface of the medium, S), capillarity can no longer sustain viscous flow, and the films detach from the external surface of the medium. The film tips, which now act as a moving evaporation front, recede deeper in the pore space, leaving behind an increasing completely dry region of pores just below the surface of the medium (Yiotis et al. 2012b). Given that the effective diffusivity within the material is much lower than over the external surface S, this period is controlled by diffusive mass transfer through the increasingly larger dry region, resulting into a decreasing recovery rate.

When gravity enhances drying, namely when film flow is in the same direction as the gravity acceleration vector, the situation is likely to be different. Here, for sufficiently slow external mass transfer, the gas–liquid front is expected to become unstable and, almost from the onset, form a gravity finger of gas that reaches the bottom (closed to the ambient) side of the medium immediately upon the start of the process. This leads to a prolonged presence of the bulk liquid phase just below the product surface (as far-field pores are preferably invaded) and results in a process characterized by a CRP only. One-dimensional considerations in previous studies (Yiotis et al. 2012a, b) established the condition, $\mathrm{Ca_f Sh} < 3\mathrm{Bo}$, for the above case. However, if the external mass transfer is sufficiently fast, a scenario similar to that for the gravity-opposing case described above is also possible when $\mathrm{Ca_f Sh} > 3\mathrm{Bo}$. Namely, a stable evaporation front may develop, which will recede in the medium following the underlying percolation front (which could, however, remain unstable). We will test these 1-D predictions in the present contribution using pore network modeling for the more general 3-D case, and where the pore sizes are spatially disordered.

Pore network modeling of drying in porous media has proven to be a powerful methodology to study the pore-scale heterogeneity and transport mechanisms and their impact on the macroscopic behavior of the process. Originally developed by Fatt (1956), the method has evolved from simple percolation theory (Prat 1993, 1995), to models that include corner film flow (Yiotis et al. 2004; Prat 2007) and, more recently, the added effect of an external mass transfer boundary layer (Yiotis et al. 2007), thus capturing increasingly more complex phenomena. Still lacking, however, are certain effects identified in recent studies in model 1-D geometries (e.g., single-capillary tubes (Chauvet et al. 2009, 2010) or packed bead packings (Yiotis et al. 2012a, b)) to play an important role. These studies demonstrated important effects of gravity, pore wall roundness and external mass transfer on the extent of the film region and on the drying rates.

In our recent contributions (Yiotis et al. 2012a, b), we proposed an analytical solution for the drying of a 1-D porous medium, where the complicated interplay of gravity, capillarity, external mass transfer conditions and corner roundness were all accounted for in order to predict the transition from the CRP to FRP regimes and successfully recover the corresponding drying curves. Despite the fact that our model compared very favorably with experimental results of drying bead packings in the case of gravity-opposed drying and in the limit of relative high Bo numbers (Yiotis et al. 2012b), such a 1-D approach essentially ignored the effects of pore-scale disorder that may lead to a gradual desaturation of the product surface, and thus a smoother transition between the above two periods of drying, as opposed to the sharp transition predicted by the 1-D model.

The objective of this contribution is thus to extend previous pore network models to also account for the above effects on drying, thus providing a model that includes all major mechanisms experimentally identified to play an important role. The model will account for viscous flow through liquid films, gravity, and mass transfer both within the dry medium and also through the mass boundary layer over the external surface of the medium. We will also discuss effects of pore wall microstructure through an assumed spatially uniform parameter p, the degree of corner roundness, that appears to have a notable effect on the extent of the film region (Chauvet et al. 2010).

2 Model Formulation

We proceed by postulating, as in previous studies (Yiotis et al. 2003, 2012b), that drying entails the following four regions;

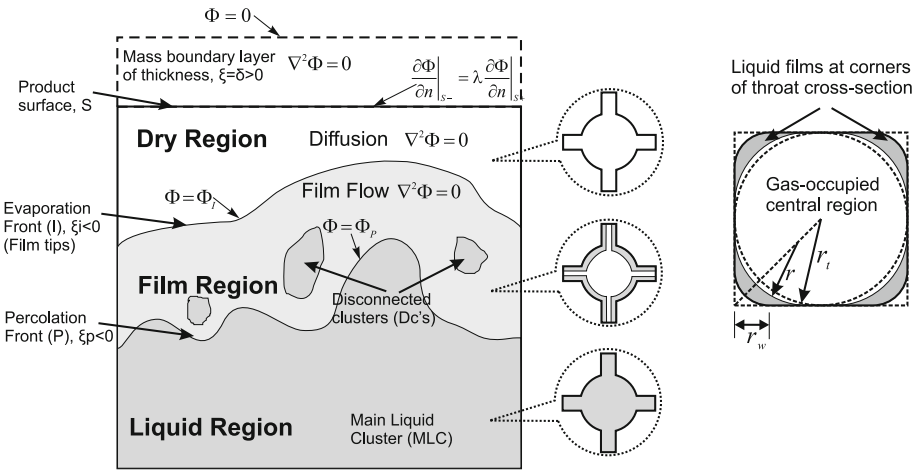

Fig. 1 (*Left*) Schematic of the characteristic pore regions encountered during drying of macroporous media. (*Right*) Cross-sectional area of a film-occupied square throat with rounded corners

1. A liquid region that covers initially the entire domain and contains only liquid-saturated pores (shown in darker gray color in Fig. 1). The largest liquid-saturated region is denoted as the main liquid cluster (MLC), while smaller liquid clusters, that detach from the initial MLC, are denoted as disconnected clusters (DC's).
2. A film region (shown in lighter gray color) that consists of pores invaded by the gas phase, but of whose pore walls are still covered by a continuous liquid film that allows for flow between liquid clusters (either DC's or the MLC) and the product surface, S, which is open to the environment. Here, the gas phase in the central part of the pores is saturated by the vapors of the volatile species, and thus there is negligible evaporation within these pores (e.g., see Eijkel et al. 2005), as well as negligible diffusive mass transfer within this region.
3. A completely dry region (shown in white color below S), where the pore bodies are completely dry and do not contain any continuous films. It is through this region, where diffusive mass transfer takes place at rates proportional to the effective diffusivity of the porous medium, $D_{\text{eff},S-}$ (Yiotis et al. 2012b).
4. Finally, a mass boundary layer covers the external surface of the medium (shown in white color above S), whose thickness depends on local flow conditions, and where we denote the bulk phase effective diffusivity of the vapors of the volatile species by $D_{\text{eff},S+}$.

We denote the interface between the liquid region and the film region as the percolation front (P), and the interface between the film region and the dry region as the evaporation front (I), since it is there where vaporization of the liquid species predominantly takes place (see Fig. 1).

Given that mass transport is primarily through viscous corner flow in the film pore region and diffusion through both the dry pore region of the porous medium, but also within the mass boundary layer, we propose in the following sections the mathematical formulation for a single scalar variable, Φ, whose spatially continuous gradients describe mass fluxes in all pore regions, in a similar fashion as in Yiotis et al. (2003). We then express mass transport in pore throats as gradients of Φ, multiplied by the throat cross-sectional area, by imposing appropriate boundary conditions for Φ at the percolation front (P), where the films emanate,

and at the top of mass boundary layer, where we impose $\Phi = 0$. A pore network model based on this formulation is developed in Sect. 3.

2.1 Mass Transport in the Film Region

In the film region, we model film flow in the cavities of the porous medium in analogy to corner flow through films that form at the corners of capillaries with noncircular cross-section (e.g., a square capillary) (Dong and Chatzis 1995; Eijkel et al. 2005; Chauvet et al. 2009). There, flow is driven by both gravity and the gradient in the capillary pressure, $P_l = -\gamma/r$, where γ is the interfacial tension and r is the radius of curvature of the film (and where without loss we take the gas pressure to be zero).

Following Ransohoff and Radke (1988), Dong and Chatzis (1995), the volumetric flow rate across the cross-section of the capillary of size $2r_t$ is;

$$Q_x = -\frac{C^*\gamma}{\mu_l \beta}\left(r^2\frac{\partial r}{\partial x} - \frac{r^4 \rho_l g_x}{\gamma}\right) \tag{1}$$

or equivalently;

$$Q_x = -\frac{\gamma r_t^2}{\mu_l}\left(f(\rho)\rho^2\frac{\partial \rho}{\partial \xi} - \mathrm{Bo} f(\rho)\rho^4\right) \tag{2}$$

where μ_l and ρ_l are the liquid-phase viscosity and density, respectively, g_x is the gravity acceleration component in the flow direction, $\rho = r/r_t$ is the dimensionless film thickness, $\xi = x/r_t$ is the dimensionless distance from the product surface, and $\mathrm{Bo} = \frac{g_x \rho_l r_t^2}{\gamma}$ is the Bond number. Here we introduced a function, $f(\rho) = C^*/\beta$ that describes the hydraulic conductivity of the corner films, where $C^* = (4-\pi)(1-(p/\rho)^2)$ is the cross-sectional area available for flow and $\beta = \beta(\rho)$ is a dimensionless resistance to flow. The latter function is obtained using a least-square fit on the data calculated by Dong and Chatzis (1995) for a square capillary with rounded corners. The corner roundness is defined by the parameter $p = r_w/r_t$, where r_w is the corner radius of curvature (See Fig. 1 for a schematic of the corner flow process).

Equation 2 can be conveniently expressed in the form of a gradient of a scalar variable as follows;

$$\begin{aligned} Q_x &= -\frac{\gamma r_t^2}{\mu_l}\frac{\partial}{\partial \xi}\left(\int_p^\rho f(\rho^*)\rho^{*2}\mathrm{d}\rho^* - \mathrm{Bo}\int_{\xi_i}^{\xi} f(\rho)\rho^4 \mathrm{d}\xi^*\right) \\ &= -\frac{\gamma r_t^2}{\mu_l}\frac{\partial}{\partial \xi}\left(J(\rho) - \mathrm{Bo} Ix(\xi)\right) \end{aligned} \tag{3}$$

where ξ_i is the dimensionless location of the film tips [i.e., the average position of the evaporation front (I)], and we denote the two integrals as;

$$J(\rho) = \int_p^\rho f(\rho^*)\rho^{*2}\mathrm{d}\rho^* \tag{4}$$

and

$$Ix(\xi) = \int_{\xi_i}^{\xi} f(\rho)\rho^4 \mathrm{d}\xi^*. \tag{5}$$

Equation 3 describes film flow at the corners of a single capillary and can be readily extended to 3-D by considering mass conservation in a network of intersecting capillaries, as follows;

$$\nabla^2(J(\rho) - \mathrm{Bo}Ix(\xi)) = -\mathrm{Bo}\left(\frac{\partial^2}{\partial u^2}\int_{\xi_i}^{\xi} f(\rho)\rho^4 \mathrm{d}\xi^* + \frac{\partial^2}{\partial \omega^2}\int_{\xi_i}^{\xi} f(\rho)\rho^4 \mathrm{d}\xi^*\right) \tag{6}$$

where $u = y/r_\mathrm{t}$ and $\omega = z/r_\mathrm{t}$.

The right-hand side of Eq. (6) is negligible, as long as fronts are stabilized (e.g., by gravity), or far from the percolation front (Tajer 2011), and we can thus write the above mass conservation equation as;

$$\nabla^2(J(\rho) - \mathrm{Bo}Ix(\xi)) = 0 \tag{7}$$

2.2 Mass Transport in the Dry Region

In the completely dry pore region of the medium and the mass bounday layer over the product surface, mass transfer is assumed through steady-state diffusion. Therefore, mass conservation reads;

$$\nabla \cdot j = D_M \nabla^2 C = 0 \tag{8}$$

where j is the diffusive mass flux, D_M is the molecular diffusivity and C is the vapor concentration of the volatile species. We should note here that the effective (volume-averaged) diffusivity in the porous medium (previously defined as $D_{\mathrm{eff},S-}$) is always lower than the effective diffusivity over the product surface (defined as $D_{\mathrm{eff},S+}$), due to the porosity and tortuosity of the porous material. This is accounted for in the pore network model presented in Sect. 3 by appropriately adjusting the pore-throat cross-section ratio above and below the product surface (See also Eq. (15) below).

2.3 Coupled Solution in the Film and Dry Regions

The dry and film pore regions are coupled through mass conservation at the evaporation front (I) (or equivalently at the film tips), where we assume that the corner film flow reaches due to capillary pressure gradients, evaporates and then diffuses on the dry side of the front. Thus, mass conservation at I reads;

$$\rho_\mathrm{l} Q_n = -4r_\mathrm{t}^2 D_M C_e \frac{\partial \zeta}{\partial n} \tag{9}$$

where Q_n is the film flow rate in the normal direction to the front I, $4r_\mathrm{t}^2$ is the throat cross-section (note that r_t is the throat 'radius', not to be confused with the film thickness r), $\zeta = C/C_e$ and C_e is the equilibrium (at vapor pressure) concentration of the volatile species.

Using Eqs. (3) and (9), and taking the direction x as the normal to the evaporation front, we have

$$\frac{\partial\,(J(\rho))}{\partial \xi} = \mathrm{Ca}_\mathrm{f}' \frac{\partial \zeta}{\partial \xi} \tag{10}$$

Here we defined a film-based capillary number $\mathrm{Ca}_\mathrm{f}' = \frac{4\mu_\mathrm{l} D_M C_e}{\rho_\mathrm{l}\gamma r_\mathrm{t}}$ (which is within a geometric constant of order 1 similar to our previous definition (Yiotis et al. 2012b), $\mathrm{Ca}_\mathrm{f}' = \frac{4}{3\pi}\mathrm{Ca}_\mathrm{f}^*$).

The above rearrangements allow us to introduce the following transformation that captures in a single scalar variable, Φ, mass transport through both the film and dry regions;

$$\Phi = \frac{J(\rho) - \mathrm{Bo}Ix(\xi) + \mathrm{Ca}_\mathrm{f}'\zeta}{J_p + \mathrm{Ca}_\mathrm{f}'} \tag{11}$$

where

$$J_p \equiv J(\rho = 1) = \int_p^1 f(\rho^*)\rho^{*2}\mathrm{d}\rho^* \tag{12}$$

Note that the denominator of Eq. (11) is selected in such a way so that $\Phi = 1$ at the percolation front, P, in the limit when $\mathrm{Bo} = 0$.

Then, Φ satisfies the Laplace equation, $\nabla^2\Phi = 0$ (in the case when Φ is continuous at the product surface), in both the film and dry regions within the porous medium, but also above the external surface S within the mass boundary layer. Its solution will allow us to account comprehensively for all relevant effects, namely gravity, capillarity, viscosity and pore wall microstructure.

The variable Φ is subject to the following boundary conditions;
At the percolation front P, where the films emanate, we have $\zeta = 1$ and $\rho = 1$, hence;

$$\Phi_P = 1 - \frac{\mathrm{Bo}}{J_p + \mathrm{Ca}_\mathrm{f}'} Ix(\xi_p) \tag{13}$$

Note that the above boundary condition assumes a radius of curvature equal to r_t at the percolation front where the films emanate. A more elaborate study on the exact shape of the bulk liquid menisci can be found in Wong et al. (1992).

At the evaporation front I, conditions $\zeta = 1$ and $\rho = p$ apply (assuming that it lies within the porous medium), therefore;

$$\Phi_I = \frac{\mathrm{Ca}_\mathrm{f}'}{J_p + \mathrm{Ca}_\mathrm{f}'} \tag{14}$$

The latter equation determines the position of the film tips, which in addition to being a function of the film-based capillary number Ca_f', as also was the case in our previous works, it also depends here on J_p, as well. The latter parameter accounts for the effects of corner roundness in pore throats.

At the top of the mass boundary layer, the conditions $\rho = 0$ and $\zeta = 0$ apply, thus $\Phi = 0$. Note that the thickness of the mass boundary layer depends on local flow conditions through an appropriately defined Sherwood number, as we will discuss in more detail below.

At the beginning of the drying process, where the films reach all the way up to the product surface, the solution for Φ is discontinuous at S, with a finite film thickness ρ^* on the porous medium side S- and a zero film thickness on the external side S+, corresponding to Φ_I. The mass flux, however, remains continuous at S;

$$\left.\frac{\partial\Phi}{\partial\xi}\right|_{S-} = \lambda \left.\frac{\partial\Phi}{\partial\xi}\right|_{S+} \tag{15}$$

Here, $\lambda = \frac{D_{\mathrm{eff},S+}}{D_{\mathrm{eff},S-}} > 1$ is the ratio of external to internal effective (volume-averaged) diffusivities. An approximation for λ can be obtained through $\frac{D_{\mathrm{eff},S+}}{D_{\mathrm{eff},S-}} = \frac{\tau}{\phi}$, where τ and ϕ are the tortuosity and porosity of the medium, respectively. In the pore network model developed in the following section, λ is implemented as the ratio of the average throat cross-section within the porous medium to the cross-section of throats above the product surface. At later times, when the film tips have detached from the product surface, Eq. (15) remains valid, but now the Φ profile becomes continuous at S (Yiotis et al. 2012a).

Before we proceed further, it is worth noting the dependence of $J(\rho)$ and J_p in the transformation of Eq. (11) on the degree of roundness in order to obtain insight into the effects of p on the extent of the film region and the corresponding position of the evaporation front as defined by Eq. (14). In interpreting these results, it is worth recalling that Ca_f' is typically

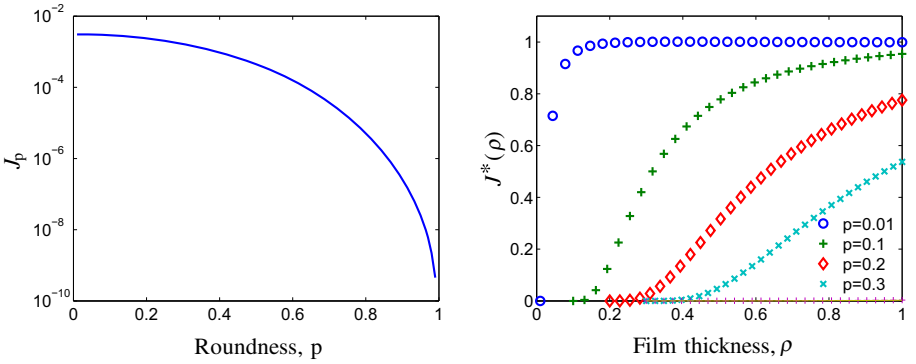

Fig. 2 Variation of the transport integrals in Eqs. (11) and (14) with the degree of corner roundness, p. (*Left*) J_p versus p; (*Right*) Effects of corner roundness along a single capillary (for a film thickness ranging from $\rho = 1$ at the percolation front to $\rho = 0$ at the evaporation front) for fixed values of the corner roundness, p. The results are normalized with the sharp corner value as $J^* = J(\rho; p)/J(\rho; 0)$

of the order of 10^{-6}. Figure 2-(Left) shows that in the limit where $p \to 0$, namely for sharp corners, J_p becomes practically independent of p, and thus the extent of the film region is solely determined by Ca_f', as in Yiotis et al. (2003). In the opposite limit of rounded corners, when $p \to 1$, then $J_p \to 0$, leading thus to extremely short films and an evaporation front that practically collapses to the percolation front ($\Phi_I = \Phi_P = 1$) in the case of negligible gravity, $\mathrm{Bo} = 0$.

Figure 2-(Right) shows the effects of corner roundness along a single capillary (for a film thickness ranging from $\rho = 1$ at the percolation front to $\rho = 0$ at the evaporation front) for fixed values of the corner roundness, p. The results are normalized with the sharp corner value as $J^* = J(\rho; p)/J(\rho; 0)$. For $p \ll 1$ there is a significant effect only close to the film tips. However, film-long effects become significant if p is not very small (for values as low as 0.1).

3 Pore Network Modeling

Pore network models of transport processes in porous media have been employed successfully in the last couple of decades. Although with significant computational demands, these treat transport processes at the pore network scale, thus offering the additional detail required to solve problems over a wider range of flow conditions, while also providing tools for relating pore-scale phenomena to the 'effective', continuum-scale behavior (Blunt et al. 2002).

Typically, the porous medium is treated as a lattice of larger pore bodies (voids) interconnected through narrower throats of various sizes and shapes. Pore bodies serve as phase containers, with typically negligible contribution to flow resistance and mass transfer, while the throats serve primarily as flow and transport resistors, with negligible phase capacity. The predictive capabilities of the approach depend strongly on the construction of accurate, representative networks of pores, a field of active research (Wildenschild and Sheppard 2013; Gostick 2013). A set of transport equations, e.g., viscous flow equations of motion or Ficks equation for diffusive mass transfer, are then solved within discrete networks of pores and throats.

In this paper, we will assume a fixed topology, taken as a 3-D cubic network of spherical pores interconnected through throats with a square cross-section, but with rounded corners

[See Fig. 1-(Right)]. The mass boundary layer over the medium is also approximated using a cubic network of larger 'pseudo-pores' and throats to match the volume and cross-section of the actual boundary layer. The ratio of effective (volume-averaged) diffusivities above and below the product surface, λ, is implemented by appropriately adjusting the ratio of the throat cross-section, as $\lambda = \frac{D_{\mathrm{eff},S+}}{D_{\mathrm{eff},S-}} = \frac{r_{\mathrm{t},S+}^2}{\bar{r}_\mathrm{t}^2} > 1$, where $r_{\mathrm{t},S+}$ is the fixed throat radius in the mass boundary layer and $\bar{r}_\mathrm{t}$ is the average throat radius within the porous medium.

In integrating the conservation equations for flow and mass transfer over a pore body of volume $V_\mathrm{p} = \frac{4}{3}\pi r_\mathrm{p}^3$, where r_p is the pore body radius, we use the identity

$$\int_{V_\mathrm{p}} (\nabla \cdot j)\,\mathrm{d}V = \oiint_{A_\mathrm{t}} (n \cdot j)\,dA \tag{16}$$

where $j \propto \nabla\Phi$ is the flux in the corresponding film or dry region, and n is the unit vector normal to the surface of the throats cross-section, A_t. For the film and dry regions and for the mass diffusion layer over the medium, Eqs. (7), (8), (11) and (16) give

$$\sum_j \rho_{\mathrm{t},ij}^2 \left(\Phi_i - \Phi_j\right) = 0 \tag{17}$$

where $\rho_{\mathrm{t},ij} = r_{\mathrm{t},ij}/\bar{r}_\mathrm{t}$ is the normalized throat 'radius' between adjacent pore bodies i and j.

Application of the above equation in all pore bodies within the film, dry and mass boundary regions leads to a system of linear equations for Φ to be solved subject to the appropriate boundary conditions at the percolation front and the top of the mass boundary layer, as shown in Fig. 1. The overall drying rate j_e is then calculated by integrating the gradient of Φ at the top of the external mass boundary layer, located at distance δ from the product surface, using the outer boundary condition $\Phi = 0$;

$$j_e = -\frac{D_{\mathrm{eff},S+}C_e}{\bar{r}_\mathrm{t}} \int_A \frac{\partial\zeta}{\partial\xi}\mathrm{d}A = \frac{4D_{\mathrm{eff},S+}C_e\bar{r}_\mathrm{t}^2}{l\Phi_I} \sum_j \rho_{\mathrm{t},ij}^2 \Phi_j \tag{18}$$

where l is the distance between pore centers.

The above drying rate is partitioned between individual liquid clusters (both the MLC and DC's) depending on the gradient of Φ at the perimeter of each cluster (percolation front), as follows;

$$j_{e,cl} = j_e \frac{\int_{A,cl} \frac{\partial\Phi}{\partial n}\mathrm{d}A}{\sum_{i=1}^{N} \left(\int_{A,i} \frac{\partial\Phi}{\partial n}\mathrm{d}A\right)} \tag{19}$$

where n is the unit vector at the perimeter, the index cl denotes individual clusters and N is the total number of liquid clusters.

At the beginning of the process, all pore bodies below the product surface are saturated by the volatile liquid, which in our simulations is hexane (See Table 1 for physical properties).

Table 1 Physical properties of n-hexane

Liquid density, ρ_l	660 kg/m^3
Liquid viscosity, μ_l	0.31 mPa /s
Surface tension, γ	18.43 mN/m
Equilibrium Gas phase concentration, C_e	0.67 kg/m^3
Diffusion coefficient, D_M	8.9×10^{-6} m^2/s

The liquid evaporates at all evaporation interfaces, with the vapor diffusing through the gas phase (if any) toward the top of the external surface. We assume that external and internal mass transfer are decoupled in the sense that the thickness of the boundary layer remains constant in time, and the concentration of the vapor is zero at the outer edge of that layer ($\zeta = 0$ or, equivalently, $\Phi = 0$).

As the liquid evaporates, the gas phase enters the pore space through the interface throats with the minimum capillary pressure, P_c, at the perimeter of each liquid cluster (percolation front) where the films emanate. The local capillary pressure is calculated as;

$$P_{c,ij} = P_g - P_l = 2\frac{\gamma}{r_{t,ij}} + \rho_l g_x x \tag{20}$$

where the indices ij denote neighboring pores across the percolation front. Here $x < 0$, and $g_x > 0$ for the case of a gravity-stabilized front, $g_x < 0$ for the case of gravity-enhancing drying.

All partially empty pores are then emptied simultaneously, within a time interval δt, assuming a constant local rate $j_{e,cl}$. The time interval is selected such that it is just sufficient for one liquid pore (located at the percolation front over the MLC and all DC's) to become fully empty. This actually corresponds to a transition from a liquid saturated to a film pore. However, the liquid contained in the form of corner films is considered to be negligible compared with the bulk liquid saturation, and it is thus not accounted for in our calculations. The liquid saturation, S_i, of each partially empty pore is then calculated as;

$$S_i^{t+\delta t} = S_i^t - \frac{j_{e,cl}}{\rho_l V_{p,i}}\delta t \tag{21}$$

The receding of the percolation fronts is realized using a Hoshen–Kopelman algorithm (Hoshen and Kopelman 1976) at each time step in order to identify all macroscopically isolated liquid clusters (the MLC and DC's), and to also identify the perimeter of each one. A pore located at the perimeter of each identified cluster (adjacent to the throat with the minimum capillary pressure) is selected and emptied at a drying rate proportional to the surface integral of the gradient of Φ at the perimeter of the corresponding cluster (calculated by Eq. (19). The spatial profile of Φ is determined by the solution of Eq. (17), using the boundary conditions Φ_P at the percolation front [as calculated from Eq. (13)] and $\Phi = 0$ at top of the mass boundary layer δ. While the number of pores that empty simultaneously is equal to the number of isolated liquid clusters, each pore empties at its own rate. When the first liquid pore becomes completely dry (namely a film pore), the whole process is repeated to identify the newly formed isolated liquid clusters, the percolation front, the next pore throat to be invaded, and so on.

For the solution of the Laplace equation for Φ in the dry and film pores [Eq. (17)], we employ an iterative solver based on a complex successive over-relaxation (SOR) scheme (see e.g., Young 1971). Note, however, that in the presence of gravity, Bo $\neq 0$, the boundary condition for Φ at the percolation front is not fixed a-priori [see Eq. (13)]. Rather, it is a function of the integral $Ix(\xi)$, which in turn requires the exact solution for the film thickness ρ (and thus Φ) (in contrast to the case in the absence of gravity where Bo $= 0$ and thus $\Phi_P = 1$). An implicit scheme based on two nested iterative SOR solvers is used: The inner solver handles the Laplace equation and converges toward an approximate solution for Φ based on the estimated value of $Ix(\xi)$ (and thus the boundary condition Φ_P) provided by the outer solver. The outer solver then relaxes toward a new estimate for $Ix(\xi)$ (and thus Φ_P) based on the previous estimate for $Ix(\xi)$ and the current estimate for Φ from the inner loop.

The iterative process is terminated when a convergence criterion is satisfied for both $Ix(\xi)$ and Φ.

A short outline of the pore network model algorithm proposed in this study is the following:

1. Starting from an initial spatial distribution of fully liquid pores, a Hoshen–Kopelman clustering algorithm is employed to identify all isolated liquid clusters (the MLC and DC's) and the liquid pores at the perimeter of each cluster.
2. If all liquid pores of a cluster are fully saturated by liquid (namely, there does not exist a liquid pore at the perimeter of the cluster that has been partially emptied at a previous time), the throat with the minimum capillary pressure threshold is identified, according to Eq. (20), and the corresponding liquid pore is then invaded by the gas phase.
3. The Laplace equation for Φ is solved [Eq. (17)] in order to locate the position of the evaporation front (film tips) and identify film and dry pore regions.
4. The overall evaporation rate is calculated using Eq. (18).
5. The evaporation rate from each cluster is calculated using Eq. (19).
6. The time δt required to empty a partial empty liquid pore at the percolation front along the perimeter of all clusters is calculated.
7. The saturation of all partially empty liquid pores at the percolation front is updated assuming a constant evaporation rate during a time interval δt [Eq. (21)], and the algorithm returns to the first step until a criterion for the residual liquid saturation is satisfied.

4 Results and Discussion

We performed a series of numerical simulations with 2-D square and 3-D cubic regular pore networks in order to study a number of effects, including gravity, corner roundness and mass boundary layer thickness on the drying curves and the underlying phase distribution patterns. All lateral and bottom sides of the pore network were closed to flow and mass transfer, while the top side was open to the mass transfer boundary layer, as shown in Fig. 1. The pore and throat sizes in the network followed a Gaussian distribution with an average value $\bar{r}_\mathrm{p}$ and $\bar{r}_\mathrm{t}$, and standard deviations σ_p and σ_t for the pores and throats, respectively. The throat size within the mass boundary layer was fixed according to $r_{\mathrm{t},S+} = \sqrt{\lambda}\bar{r}_\mathrm{t}$ in order to match the required ratio of effective diffusivities above and below S. Pore network characteristics are shown in Table 2. We note here that other common size distributions, such as a Gamma, are equally feasible in our model.

Table 2 Pore network characteristics for the numerical simulations of this study

Connectivity 2-D	2-D square regular lattice, connectivity 4
Connectivity 3-D	3-D cubic regular lattice, connectivity 6
Distribution	Gaussian for pores and throats
Distance between pore centers, l	500 μm
Mean pore radius, $\bar{r}_\mathrm{p}$	250 μm
Standard deviation of pore radii, σ_p	5 μm
Mean throat radius, $\bar{r}_\mathrm{t}$	60 μm
Standard deviation of throat radii, σ_t	0.1–10 μm
Throat radius in the mass boundary layer, $r_{\mathrm{t},S+}$	$r_{\mathrm{t},S+} = \sqrt{\lambda}\bar{r}_\mathrm{t}$

Effects of gravity, capillarity and mass boundary layer are expressed in terms of the three dimensionless numbers: A film-based capillary number $\mathrm{Ca}'_{\mathrm{f}}$ (again not to be confused with Ca_{f} defined in Yiotis et al. (2012a) for a square capillary with sharp corners), that expresses the ratio of viscous forces to capillary forces in the films;

$$\mathrm{Ca}'_{\mathrm{f}} = \frac{4\mu_{\mathrm{l}} D_M C_e}{\rho_{\mathrm{l}} \gamma \bar{r}_{\mathrm{t}}} \tag{22}$$

The Bond number, Bo, that expresses the ratio of gravity to capillary forces;

$$\mathrm{Bo} = \frac{g_x \rho_{\mathrm{l}} \bar{r}_{\mathrm{t}}^2}{\gamma}, \tag{23}$$

and a Sherwood number, Sh, that describes mass transfer conditions within the mass boundary layer over the product surface, defined as;

$$\mathrm{Sh} = \frac{\lambda}{\delta} = \frac{\lambda \bar{r}_{\mathrm{t}}}{\Delta}, \tag{24}$$

where Δ is the thickness of the mass boundary layer and $\delta = \Delta/\bar{r}_{\mathrm{t}}$ is its corresponding dimensionless value.

An additional important parameter is the disorder of the throat size distribution, expressed in dimensionless notation by $\Sigma_{\mathrm{t}} = \sigma_{\mathrm{t}}/l$, where l is the distance between the pore centers. The mean position and the width of the percolation front of the main liquid cluster (the largest liquid cluster of the domain) were defined as follows;

$$\bar{\xi}_{pf} = \frac{\int_\xi \xi p_f(\xi) \mathrm{d}\xi}{\int_\xi p_f(\xi) \mathrm{d}\xi} \quad \text{and} \quad \sigma^2_{pf} = \frac{\int_\xi (\xi - \bar{\xi}_{pf})^2 p_f(\xi) \mathrm{d}\xi}{\int_\xi p_f(\xi) \mathrm{d}\xi} \tag{25}$$

where p_f is the probability to find an interface pore [namely, one belonging to the percolation front (P)] at distance ξ from the product surface, S. These can be also expressed in a more meaningful dimensionless notation with respect to the distance between pore centers, l (rather than the average throat size $\bar{r}_{\mathrm{t}}$), as $\Xi = x/l$, $\xi = \frac{l\Xi}{\bar{r}_{\mathrm{t}}}$ (e.g., $\bar{\Xi}_{pf} = \frac{\bar{r}_{\mathrm{t}} \bar{\xi}_{pf}}{l}$ and $\Sigma_{pf} = \frac{\bar{r}_{\mathrm{t}} \sigma_{pf}}{l}$). The above definition accounts only for the interface between the main liquid cluster and the film or dry pores, and does not include the interface of all disconnected clusters. Alternatively, an average position, $\bar{\xi}_{2p}$, with a standard deviation, σ_{2p}, of the front that includes all liquid clusters (MLC and DC's) can also be defined.

4.1 Validation

To validate the pore network model proposed in this contribution we compare our numerical results with the 1-D solution presented in one of our previous studies (Yiotis et al. 2012a, b), using a 2-D simulation in the case when gravity is strong and opposing drying, and when the pore-throat disorder is relatively small, so that the percolation front is practically flat (and thus the problem reduces to a 1-D equivalent). We should note here that our earlier 1-D solution compared very favorably with experimental results of drying glass bead packings using a single adjustable parameter to account for the corner roundness of the medium (Yiotis et al. 2012b). The 1-D solution however does not capture the gradual desaturation of the product surface due to the disorder of the underlying percolation front, which for lower values of the Bo number and high values of the pore-throat disorder, Σ_{t}, would lead to smoother transitions between the CRP and the FRP. This effect is captured using the proposed pore network model.

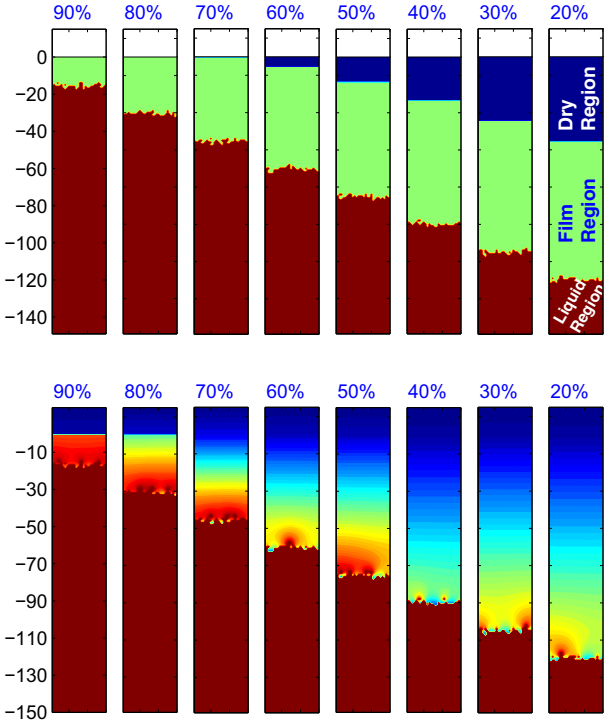

Fig. 3 2-D simulations in a 150 × 30 pore network at different times and values of the liquid saturations S, shown above each figure. (*Top*) Phase distribution patterns: Mass Boundary Layer (*White*), Dry Region (*Blue*), Film region (*Green*), Liquid region (*Red*); (*Bottom*) Φ profiles. *Red color* corresponds to larger values of Φ. Note the discontinuity of Φ at the product surface for $S > 0.70$. $\delta = 15l/\bar{r}_t$, $r_t = 60 \pm 0.5\,\mu m$, $r_p = 250 \pm 5\,\mu m$, $Ca'_f = 1.01 \times 10^{-5}$, $Bo = -8.93 \times 10^{-4}$, $Sh = 2.22 \times 10^{-2}$, $\lambda = 2.77$, $p = 0.5$

Figure 3 shows the phase distribution patterns and the Φ profiles in such a 'stable' percolation front case with $Bo = -8.93 \times 10^{-4}$ and $\Sigma_t = 10^{-3}$ for different times in the process (expressed through the liquid saturation, S). At early stages, the film region (in green color in the figure) extends all the way from the percolation front to the surface of the medium, in contact with the mass boundary layer (in white color). The Φ profile is discontinuous at S, showing that the film region has a nonzero film thickness just below the product surface, S-, while the film thickness becomes equal to the corner roundness, p, on the S+ side. During this period, the product surface remains wet, and the process is controlled by mass transfer within the mass boundary layer, leading to a constant rate drying period (as also shown in Fig. 4).

For a liquid saturation slightly higher than 0.60, the film tips (evaporation front) detach from $S-$, under the effects of gravity and viscosity. The evaporation front (much flatter than the percolation front), recedes in the pore space, and a completely dry region of pores (in dark blue color) develops below $S-$. The process is now controlled by diffusive mass transfer through the developing dry region, leading to a falling rate period regime, as also shown in Fig. 4. The latter figure plots the resulting drying rate (normalized with the CRP value) and compares it with the 1-D solution of Yiotis et al. (2012b). The two results perfectly match each other, showing that the pore network closely captures the expected behavior in this

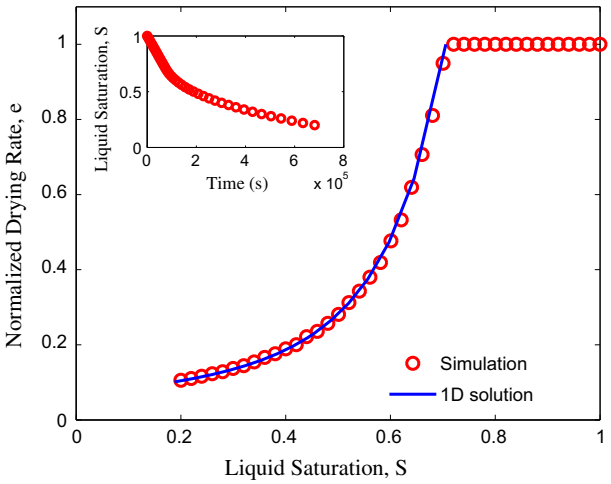

Fig. 4 Drying curve in a 2-D simulation with a 150×30 pore network model in the limit of a practically stable (*flat*) percolation front. The drying rate is made dimensionless with the corresponding CRP value. The results compare very well with the numerical solution of Yiotis et al. (2012b) (*continuous line*) for the same values of the dimensionless parameters: $\delta = 15l/\bar{r}_t$, $r_t = 60 \pm 0.5\,\mu\text{m}$, $r_p = 250 \pm 5\,\mu\text{m}$, $\text{Ca}'_f = 1.01 \times 10^{-5}$, $\text{Bo} = -8.93 \times 10^{-4}$, $\text{Sh} = 2.22 \times 10^{-2}$, $\lambda = 2.77$, $p = 0.5$

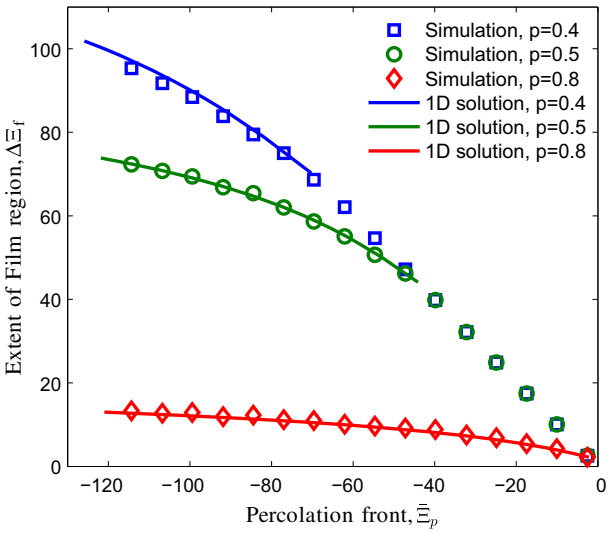

Fig. 5 Average extent of the film region $\Delta\Xi_f = \bar{\Xi}_i - \bar{\Xi}_p$ vs the average position of the percolation front $\bar{\Xi}_p$ for simulations with a 150×30 pore network at different values of the corner roundness, p. All other parameter values are the same as those of the simulation of Fig. 3. The continuous curves correspond to the numerical solution of Yiotis et al. (2012b) during the FRP only in order demonstrate the later detachment (at lower $\bar{\Xi}_p$ values) of the films from the product surface with decreasing p values, leading to increasingly longer film regions

limit. Similarly, an excellent agreement is obtained in the average extent of the film region, $\Delta\Xi_f = \bar{\Xi}_i - \bar{\Xi}_p$ as shown in Fig. 5, with the region extent increasing as the percolation front recedes deeper in the pore space. The agreement is excellent for several values of the corner roundness, p.

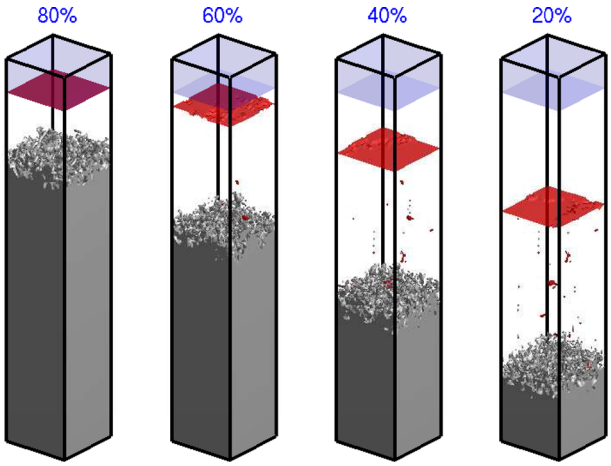

Fig. 6 Phase distribution patterns at different times in the process for a $150 \times 30 \times 30$ pore network. Liquid-saturated pores are shown in *gray color*, the position of the evaporation front is shown in *red color*, and the mass boundary layer is shown in *blue*. The corresponding liquid saturations are shown above each snapshot. $\delta = 15l/\bar{r}_t$, $r_t = 60 \pm 10\,\mu\text{m}$, $r_p = 250 \pm 5\,\mu\text{m}$, $\text{Ca}'_f = 1.01 \times 10^{-5}$, $\text{Bo} = -8.93 \times 10^{-4}$, $\text{Sh} = 2.22 \times 10^{-2}$, $\lambda = 2.77$, $p = 0.5$

4.2 Effects of Gravity and Medium Disorder when Bo < 0

Consider now the more general case of a 3-D porous medium represented by a regular cubic pore network of size $150 \times 30 \times 30$. The phase distribution patterns for a typical simulation with a more disordered medium when gravity opposes drying ($\text{Bo} = -8.93 \times 10^{-4}$ and $\Sigma_t = 2 \times 10^{-2}$) are shown in Fig. 6 for different values of the residual liquid saturation. The parameters used in this simulation will serve as the base state for the subsequent simulations. As previously, the evaporation front (red-colored surface here) remains in contact with the product surface and the mass boundary layer (transparent blue region) for $S > 0.60$. Below this saturation, the evaporation front detaches from the product surface, under the effects of gravity, and recedes in the pore space following the underlying percolation front, while a completely dry region of pores develops above the evaporation front.

In this case, an estimate of the effects of gravity and pore-throat disorder can be obtained by considering the extent (roughness) of the resulting percolation front. We anticipate that after some initial period, the percolation front thickness will scale with the Bond number and the standard deviation of the throat size distribution as;

$$\Sigma_{pf} \propto \left(\frac{|\text{Bo}|}{2\Sigma_t} \right)^{-\frac{\nu}{\nu+1}} \tag{26}$$

where the critical exponent ν comes from the Percolation theory (Chaouche et al. 1994; Tsimpanogiannis et al. 1999; Prat and Bouleux 1999).

Figure 7-(left) shows the temporal evolution of the percolation front in the pore space for various values of the parameter $\text{Bo}^* = \frac{|\text{Bo}|}{2\Sigma_t}$, corresponding to fronts of different roughness and disorder. The extent of the percolation front of the main liquid cluster is found to be practically constant with time, but remains a strong function of Bo^*. Figure 7-(right) shows that the power law dependence of Eq. (26) is nicely satisfied, although with a scaling exponent equal to 0.55, somewhat higher than the theoretical value of 0.47 for a 3-D problem. We

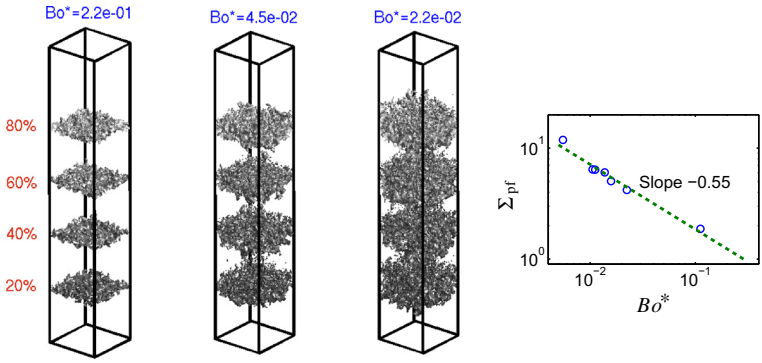

Fig. 7 (*Left*) Snapshots of the percolation front (in *gray color*) within the medium for various values of Bo* and fixed Bo $= -8.93 \times 10^{-4}$. The corresponding liquid saturations are shown on the *left* of the figure. $\delta = 15l/\bar{r}_t$, $\bar{r}_t = 60\,\mu$m, $r_p = 250 \pm 5\,\mu$m, $Ca'_f = 1.01 \times 10^{-5}$, Sh $= 2.22 \times 10^{-2}$, $\lambda = 2.77$, $p = 0.5$; (*Right*) Scaling of the percolation front with Bo^*. The slope is obtained from a single series of realizations with the same pore network at different Bo* values

believe that finite-size effects are the reason for this slight mismatch. Furthermore, a scaling of the overall two-phase region (both MLC and DC's) with the average position of the percolation front should be anticipated due to the magnitude of concentration gradients above the percolation front, as described in Tsimpanogiannis et al. (1999). This effect, however, is not clearly measurable in the finite domains of our study.

Despite the increasing disorder of the percolation fronts in Fig. 7, the overlying evaporation front remains essentially flat in our numerical simulations, even in the case of a significantly disordered percolation front. The effect of gravity, in this case of gravity-opposing drying, is thus primarily through limiting the extent of the film region, rather than through the stability (disorder) of the percolation front. These effects are demonstrated in Fig. 8 that shows the effects of gravity on the drying curves and the phase distribution patterns for a fixed disorder of the percolation front (fixed Bo* value). As the magnitude of the Bond number increases in Fig. 8-(left), the CRP is considerably diminished, which also corresponds to an earlier detachment of the evaporation front from the product surface, as shown in Fig. 8-(right). In the limiting case of very strong gravity, $|\text{Bo}| \to \infty$, the percolation front is flat and the evaporation front practically collapses to the percolation front (resulting into a negligible film region).

As we have discussed earlier, the 1-D solution of Yiotis et al. (2012b) adequately describes the drying process at sufficiently large Bond numbers that lead to relatively flat percolation fronts, but also finite extents of the film region, as shown in Figs. 4–5. Conversely, when gravity is weak, or when the porous medium disorder dominates, the process should be adequately described with the case in the absence of gravity described by Prat (1993), Furuberg et al. (1988) (although with film effects added).

The effect of gravity in the film region can be also demonstrated by plotting the average film thickness ρ_x as a function of the depth from the product surface $\Xi = x/l < 0$, defined as follows;

$$\rho_x(\Xi) = \frac{\int_{S_{yz}} \rho \mathrm{d}S}{\int_{S_{yz}} \mathrm{d}S} \tag{27}$$

where S_{yz} is a surface in the y-z plane.

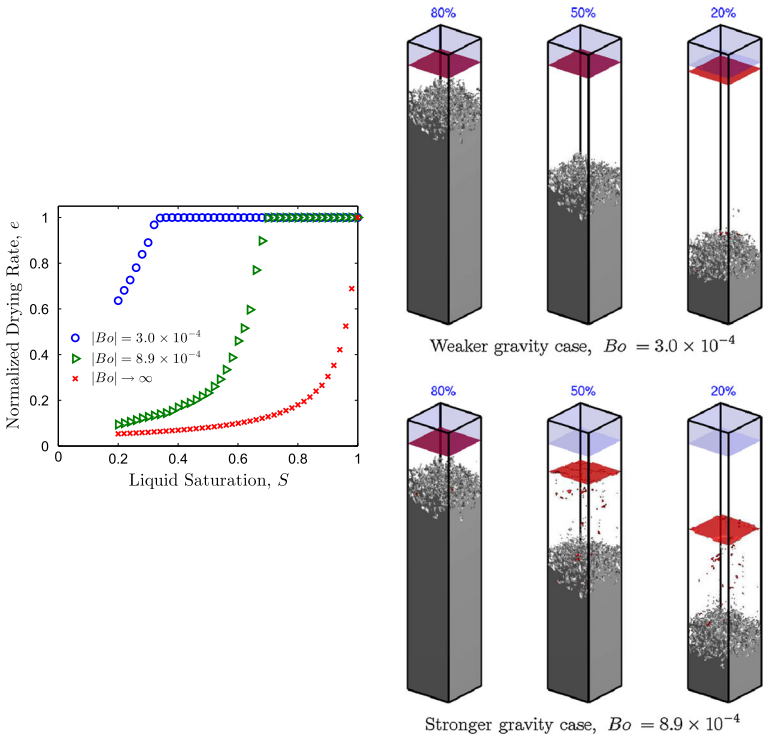

Fig. 8 Effects of gravity for fixed disorder of the percolation front, $\mathrm{Bo}^* = 2.2 \times 10^{-2}$, in 3-D simulations with a $150 \times 30 \times 30$ pore network. (*Left*) Drying curves. Also shown is the drying curve in the limit when $|\mathrm{Bo}| \to \infty$, where the percolation front is flat and the film region is absent (*red-colored curve*); (*Right*) Phase distribution patterns at various residual liquid saturations shown above each snapshot. Liquid-saturated pores are shown in *gray color*, the position of the evaporation front is shown in *red color*, and the mass boundary layer is shown in *blue*; (*Right Top*) Weaker gravity case, $\mathrm{Bo} = -3.0 \times 10^{-4}$ and $\Sigma_t = 6.6 \times 10^{-3}$, and (*Right Bottom*) a stronger gravity case, $\mathrm{Bo} = -8.9 \times 10^{-4}$ and $\Sigma_t = 2 \times 10^{-2}$. ($\delta = 15l/\bar{r}_t$, $r_t = 60\,\mu\mathrm{m}$, $r_p = 250 \pm 5\,\mu\mathrm{m}$, $\mathrm{Ca}'_f = 1.01 \times 10^{-5}$, $\mathrm{Sh} = 2.22 \times 10^{-2}$, $\lambda = 2.77$, $p = 0.5$.)

The effect is demonstrated in Fig. 9 which shows the film thickness profiles for various residual liquid saturations for two different values of Bo, but for the same disorder of the percolation front ($\mathrm{Bo}^* = 2.2 \times 10^{-2}$). Taking into account that flow through the films is driven by the combined action of capillary pressure gradients (due to gradients in film size) and gravity (see Eq. 1), this figure shows that the film thickness profiles adjust to the opposing effect of gravity in order to produce higher capillary pressure gradients and thus drive flow toward the evaporating interface. For lower Bo values [Fig. 9-(left)], the film thickness gradients, and thus the capillary pressure gradients, become smaller with a sharper decrease close to the evaporation front (film tips). The dimensionless film thickness in the film region scales as $\rho \propto \Xi^{1/3}$, as shown in our earlier studies in the absence of gravity (Yiotis et al. 2003). As Bo increases [Fig. 9-(right)], the capillary pressure gradients become larger in order to overcome the opposing effect of gravity and the film profiles are more complex. As described in the 1-D analysis (Yiotis et al. 2012a), this effect eventually leads to shorter film regions and shorter CRP's, especially in the case of fast drying conditions (i.e., high Sh numbers). The latter case will be discussed in more detail below.

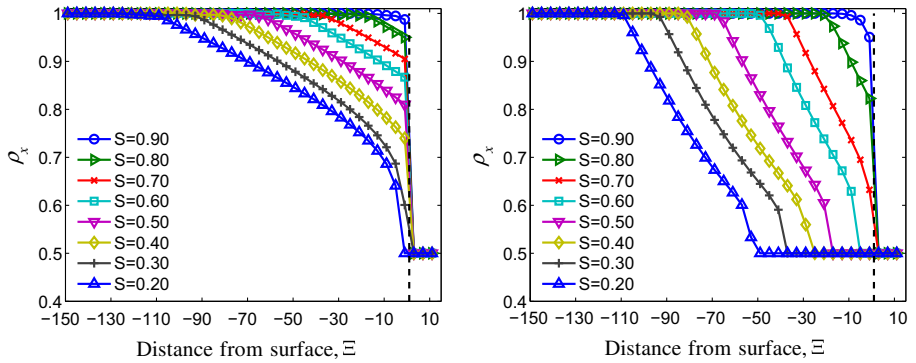

Fig. 9 Effect of gravity on the average film thickness ρ_x for the gravity-opposed case and for a fixed roughness of the percolation front (constant $\mathrm{Bo}^* = 2.2 \times 10^{-2}$). 3-D simulations with a $150 \times 30 \times 30$ pore network. (*Left*) Weaker gravity case, $\mathrm{Bo} = -3.0 \times 10^{-4}$ and $\Sigma_t = 6.6 \times 10^{-3}$; (*Right*) Stronger gravity case, $\mathrm{Bo} = -9.0 \times 10^{-4}$ and $\Sigma_t = 2 \times 10^{-2}$. ($\delta = 15l/\bar{r}_t$, $r_t = 60\,\mu\mathrm{m}$, $r_p = 250 \pm 5\,\mu\mathrm{m}$, $\mathrm{Ca}_f' = 1.01 \times 10^{-5}$, $\mathrm{Sh} = 2.22 \times 10^{-2}$, $\lambda = 2.77$, $p = 0.5$)

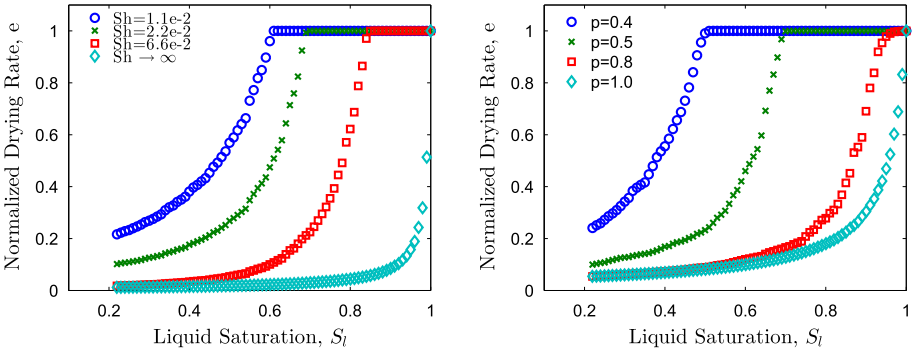

Fig. 10 Effects of Sherwood number (*Left*) and corner roundness (*Right*) on the drying curves for a $150 \times 30 \times 30$ pore network simulation. Here, $p = 0.5$ for the left panel, and $\mathrm{Sh} = 2.22 \times 10^{-2}$ for the right panel, corresponding to $\delta = 15l/\bar{r}_t$. ($r_t = 60 \pm 10\,\mu\mathrm{m}$, $r_p = 250 \pm 5\,\mu\mathrm{m}$, $\mathrm{Ca}_f' = 1.01 \times 10^{-5}$, $\mathrm{Bo} = -8.93 \times 10^{-4}$, $\lambda = 2.77$.)

4.3 Effects of Mass Boundary Layer and Corner Roundness

Of significant importance, primarily to the extent of the film region, are the effects of the external mass transfer and of the corner roundness of the pores throats. The latter affects both the area available for flow and the dimensionless resistance to flow as described by Eq. (1) (see also Chauvet et al. 2009).

Figure 10-(left) shows the effect of external mass transfer, expressed through the dimensionless mass boundary layer thickness $\delta = \Delta/\bar{r}_t$, which enters the calculations through the Sherwood number, $\mathrm{Sh} = \lambda/\delta$. For higher values of Sh, namely a thinner boundary layer, as would be the case in fast convective drying, the increased evaporative flux at the evaporation front produces higher capillary pressure gradients in the film region, and thus results in shorter films and a shorter constant rate period. The limit of infinitely fast drying has been investigated in our previous studies (Yiotis et al. 2003, 2004). Lower values of the Sh number, corresponding to a mass transfer layer of increasing thickness and slower drying, results in a

decrease in the magnitude of the capillary pressure gradients, thus allowing longer CRP's, as also shown in Yiotis et al. (2007) (although in the absence of gravity and for sharp corners).

Figure 10-(right) shows the effect of the corner roundness on the drying curves. In this case, shorter CRPs develop due both to the increased resistance to flow and to the limited cross-sectional area available for film flow, as the corner of the walls cavities become more rounded (higher p values).

4.4 Effects of Gravity when it Enhances Drying, Bo > 0

The case where gravity enhances drying can be further subdivided into two categories (Yiotis et al. 2012a), depending on the relative strengths of gravity, viscous forces and mass transfer;

1. When $3\mathrm{Bo} > \mathrm{Ca_f Sh}$, then gravity is dominant and the percolation front becomes unstable right from the onset of drying. Figure 11 shows a series of snapshots from a 2-D simulation for this case at different values of the residual liquid saturation. A single gravity finger forms that drains the fluid from the top of the medium, leaving behind in the far-field area only film-containing pores, away from the product surface, S (which is now at the bottom of the medium). Evaporation occurs at the bottom of the domain, which remains saturated by liquid practically over the entire process, thus resulting in a single continuous CRP. Note that the above condition was derived based on the assumption of sharp corners of the pore walls (namely, $p = 0$). It is straightforward to take roundness into account.
2. When $\mathrm{Ca_f Sh} > 3\mathrm{Bo}$, then gravity is weaker and a stable evaporation front, receding deeper in the pore space, can form. This occurrence is favored by stronger viscous forces (compared to gravity) and faster mass transfer in the dry region and over the product surface. Figures 12, 13 show phase distribution snapshots and the drying curve for a simulation under this condition. The drying curve in Fig. 13 exhibits first a CRP corresponding to evaporation at the product surface (now the bottom boundary) of the porous medium. This CRP is next followed by a FRP, where evaporation occurs at the film tips receding inside the porous medium. However, as the evaporation rate decreases, capillary pressure gradients in the films become progressively negligible, and the film thickness remains practically constant, and equal to $\rho = 1$ along the entire film region

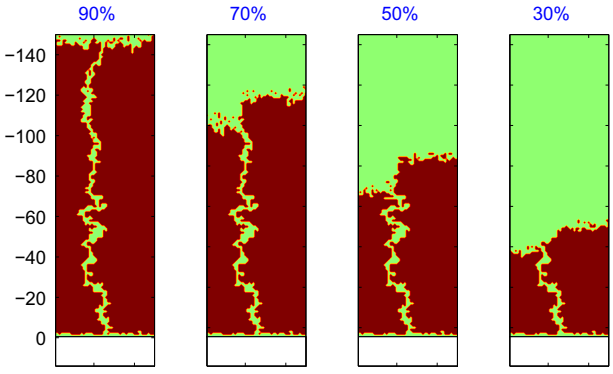

Fig. 11 Phase distribution patterns for a 150×50 pore network at different times and values of the liquid saturation, S (values shown above each snapshot), for the case when gravity enhances drying and dominates over mass transfer, namely when $3\mathrm{Bo} > \mathrm{Ca_f Sh}$. Mass Boundary Layer (*White color*), Dry Region (*Blue*), Film region (*Green*), Liquid region (*Red*). ($\delta = 15l/\bar{r}_t$, $r_t = 60 \pm 1\,\mu\mathrm{m}$, $r_p = 250 \pm 5\,\mu\mathrm{m}$, $\mathrm{Ca_f} = 2.78 \times 10^{-3}$, $\mathrm{Ca_f'} = 1.01 \times 10^{-5}$, $\mathrm{Bo} = 8.93 \times 10^{-4}$, $\mathrm{Sh} = 2.22 \times 10^{-2}$, $\lambda = 2.77$, $p = 0.4$)

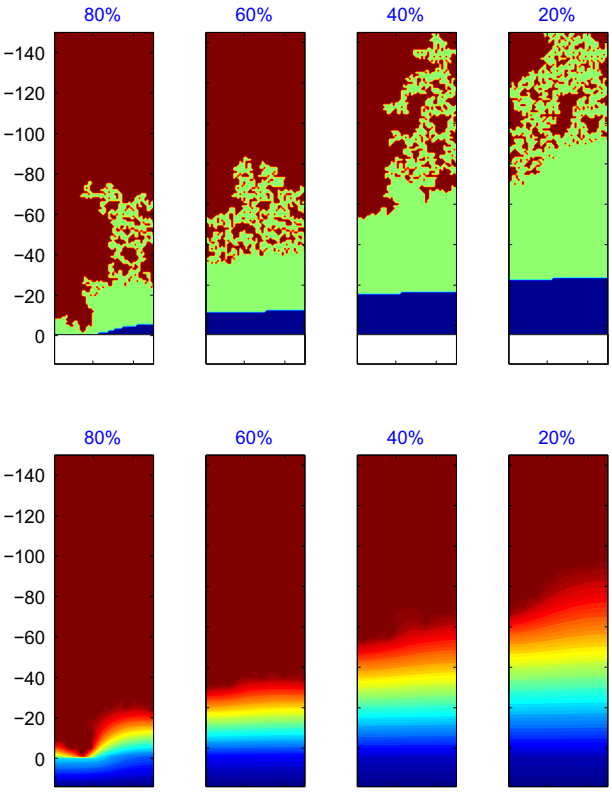

Fig. 12 2-D simulations in a 150×50 pore network at different times and values of the liquid saturations, S (values shown above each snapshot), for the case when gravity enhances drying, but when evaporation is fast enough to satisfy the condition $\mathrm{Ca_f Sh} > 3\mathrm{Bo}$. (*Top*) Phase distribution patterns: Mass Boundary Layer (*White*), Dry Region (*Blue*), Film region (*Green*), Liquid region (*Red*); (*Bottom*) Φ profile. *Red colors* show higher Φ values. ($\delta = 15l/\bar{r}_\mathrm{t}$, $r_\mathrm{t} = 60 \pm 1\,\mu\mathrm{m}$, $r_\mathrm{p} = 250 \pm 5\,\mu\mathrm{m}$, $\mathrm{Ca_f} = 1.56 \times 10^{-1}$, $\mathrm{Ca_f'} = 5.69 \times 10^{-4}$, $\mathrm{Bo} = 1.1 \times 10^{-5}$, $\mathrm{Sh} = 2.22 \times 10^{-2}$, $\lambda = 2.77$, $p = 0.4$, $\tau = 300$.)

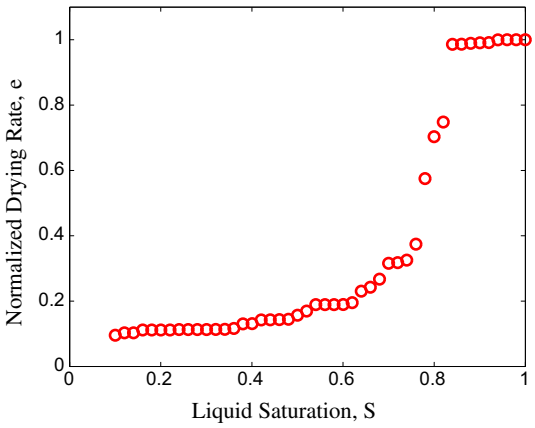

Fig. 13 Drying curve for the gravity-enhancing case in a 250×25 pore network with the "stable" condition $\mathrm{Ca_f Sh} > 3\mathrm{Bo}$ leading to two CRPs. ($\delta = 15l/\bar{r}_\mathrm{t}$, $r_\mathrm{t} = 60 \pm 0.5\,\mu m$, $r_\mathrm{p} = 250 \pm 5\,\mu\mathrm{m}$, $\mathrm{Ca_f} = 2.7 \times 10^{-1}$, $\mathrm{Ca_f'} = 1.01 \times 10^{-3}$, $\mathrm{Bo} = 1.1 \times 10^{-5}$, $\mathrm{Sh} = 2.22 \times 10^{-2}$, $\lambda = 2.77$, $p = 0.1$, $\tau = 560$)

(except very close to the evaporation front). In this case, liquid flow in the film region is driven primarily by gravity, namely by the second term on the right-hand side of Eq. (1). This leads to a situation where the evaporation front remains stationary thus leading to a constant evaporation rate, while the percolation front continuously recedes to provide for the evaporating liquid. The development of such a second CRP is clearly seen in Fig. 13, consistent with the 1-D analysis in this case (Yiotis et al. 2012a). In the present simulation, it occurs for saturations below $S < 0.4$, and corresponds to the case when gravity-driven film flow exactly balances the evaporation rate from the film tips, and capillary-driven flow is negligible.

5 Conclusion

In this contribution, we presented a pore network model for the evaporative drying of macroporous media that accounts for the major pore-scale mechanisms experimentally identified to play an important role on the drying rates and phase distribution patterns. The model accounts for viscous flow through liquid films, gravity, and for mass transfer, both within the dry medium and also through a mass boundary layer over the external surface of the medium. Also accounted are the heterogeneity of the pore size distribution and the pore wall microstructure, expressed through the degree of pore wall roundness. The model is then used to study capillary, gravity and external mass transfer effects through the variation of the appropriate dimensionless numbers. The effect of gravity is particularly analyzed, for the two cases, when gravity is opposing and when it is enhancing drying, respectively. In the latter case, when viscous forces are strong and mass transfer in the dry region fast enough compared to gravity forces, a two-CRP evaporation curve is found, as predicted by an earlier 1-D analysis. In this regime, fluid flow is driven primarily by gravity to compensate for evaporation at the film tips.

Acknowledgments The work of AGY was supported by the EU funded grant ENTEC, Contract No. 316173 under the call FP7-REGPOT.

References

Blunt, M.J., Jackson, M.D., Piri, M., Valvatne, P.H.: Detailed physics, predictive capabilities and macroscopic consequences for pore-network models of multiphase flow. Adv. Water Resour. **25**(812), 1069–1089 (2002). doi:10.1016/S0309-1708(02)00049-0

Chaouche, M., Rakotomalala, N., Salin, D., Xu, B., Yortsos, Y.C.: Invasion percolation in a hydrostatic or permeability gradient: experiments and simulations. Phys. Rev. E **49**, 4133–4139 (1994). doi:10.1103/PhysRevE.49.4133

Chauvet, F., Duru, P., Prat, M.: Depinning of evaporating liquid films in square capillary tubes: influence of corners' roundedness. Phys. Fluids **22**(11), 112113 (2010). doi:10.1063/1.3503925

Chauvet, F., Duru, P., Geoffroy, S., Prat, M.: Three periods of drying of a single square capillary tube. Phys. Rev. Lett. **103**, 124502 (2009). doi:10.1103/PhysRevLett.103.124502

Dong, M., Chatzis, I.: The imbibition and flow of a wetting liquid along the corners of a square capillary tube. J. Colloid Interface Sci. **172**(2), 278–288 (1995). doi:10.1006/jcis.1995.1253

Eijkel, J.C.T., Dan, B., Reemeijer, H.W., Hermes, D.C., Bomer, J.G., van den Berg, A.: Strongly accelerated and humidity-independent drying of nanochannels induced by sharp corners. Phys. Rev. Lett. **95**, 256107 (2005). doi:10.1103/PhysRevLett.95.256107

Fatt, I.: The network model of porous media 1–3. Pet Trans, Am Inst Min, Metall Pet Eng **207**, 144–181 (1956)

Faure, P., Coussot, P.: Drying of a model soil. Phys. Rev. E **82**, 036303 (2010). doi:10.1103/PhysRevE.82.036303

Furuberg, L., Feder, J., Aharony, A., Jøssang, T.: Dynamics of invasion percolation. Phys. Rev. Lett. **61**, 2117–2120 (1988). doi:10.1103/PhysRevLett.61.2117

Gostick, J.T.: Random pore network modeling of fibrous PEMFC gas diffusion media using Voronoi and Delaunay tessellations. J. Electrochem. Soc. **160**(8), 731–743 (2013)

Hoshen, J., Kopelman, R.: Percolation and cluster distribution. I. Cluster multiple labeling technique and critical concentration algorithm. Phys. Rev. B **14**, 3438–3445 (1976). doi:10.1103/PhysRevB.14.3438

Lehmann, P., Assouline, S., Or, D.: Characteristic lengths affecting evaporative drying of porous media. Phys. Rev. E **77**, 056309 (2008). doi:10.1103/PhysRevE.77.056309

Prat, M.: Percolation model of drying under isothermal conditions in porous media. Int. J. Multiph. Flow **19**(4), 691–704 (1993). doi:10.1016/0301-9322(93)90096-D

Prat, M.: Isothermal drying on non-hygroscopic capillary-porous materials as an invasion percolation process. Int. J. Multiph. Flow **21**(5), 875–892 (1995). doi:10.1016/0301-9322(95)00022-P

Prat, M.: On the influence of pore shape, contact angle and film flows on drying of capillary porous media. Int. J. Heat Mass Trans. **50**(78), 1455–1468 (2007). doi:10.1016/j.ijheatmasstransfer.2006.09.001

Prat, M., Bouleux, F.: Drying of capillary porous media with a stabilized front in two dimensions. Phys. Rev. E **60**, 5647–5656 (1999). doi:10.1103/PhysRevE.60.5647

Ransohoff, T.C., Radke, C.J.: Laminar flow of a wetting liquid along the corners of a predominantly gas-occupied noncircular pore. J. Colloid Interface Sci. **121**(2), 392–401 (1988). doi:10.1016/0021-9797(88)90442-0

Shaw, T.M.: Drying as an immiscible displacement process with fluid counterflow. Phys. Rev. Lett. **59**, 1671–1674 (1987). doi:10.1103/PhysRevLett.59.1671

Shokri, N., Lehmann, P., Vontobel, P., Or, D.: Drying front and water content dynamics during evaporation from sand delineated by neutron radiography. Water Resour. Res. **44**(6) (2008). doi:10.1029/2007WR006385

Suzuki, M., Maeda, S.: On the mechanism of drying of granula beds—mass transfer from discontinuous source. J. Chem. Eng. Jpn **1**, 26–31 (1968)

Tajer, E.S.: The effects of gravity and thermal gradient on the drying processes in porous media, PhD thesis, University of Southern California (2011)

Tsimpanogiannis, I.N., Yortsos, Y.C., Poulou, S., Kanellopoulos, N., Stubos, A.K.: Scaling theory of drying in porous media. Phys. Rev. E **59**, 4353–4365 (1999). doi:10.1103/PhysRevE.59.4353

van Brakel, J.: Mass transfer in convective drying. Adv. Dry. **1**, 217–268 (1980)

Wildenschild, D., Sheppard, A.P.: X-ray imaging and analysis techniques for quantifying pore-scale structure and processes in subsurface porous medium systems. Adv. Water Resour. **51**, 217–246 (2013). doi:10.1016/j.advwatres.2012.07.018

Wilkinson, D.: Percolation model of immiscible displacement in the presence of buoyancy forces. Phys. Rev. A **30**, 520–531 (1984). doi:10.1103/PhysRevA.30.520

Wong, H., Morris, S., Radke, C.J.: Three-dimensional menisci in polygonal capillaries. J. Colloid Interface Sci. **148**, 317–336 (1992). doi:10.1016/0021-9797(92)90171-H

Yiotis, A.G., Boudouvis, A.G., Stubos, A.K., Tsimpanogiannis, I.N., Yortsos, Y.C.: Effect of liquid films on the drying of porous media. AIChE J. **50**(11), 2721–2737 (2004). doi:10.1002/aic.10265

Yiotis, A., Boudouvis, A., Stubos, A., Tsimpanogiannis, I., Yortsos, Y.: Effect of liquid films on the isothermal drying of porous media. Phys. Rev. E **68**, 037303 (2003). doi:10.1103/PhysRevE.68.037303

Yiotis, A.G., Tsimpanogiannis, I.N., Stubos, A.K., Yortsos, Y.C.: Coupling between external and internal mass transfer during drying of a porous medium. Water Resour. Res. **43** (2007). doi:10.1029/2006WR005558

Yiotis, A.G., Salin, D., Tajer, E.S., Yortsos, Y.C.: Analytical solutions of drying in porous media for gravity-stabilized fronts. Phys. Rev. E **85**, 046308 (2012a). doi:10.1103/PhysRevE.85.046308

Yiotis, A.G., Salin, D., Tajer, E.S., Yortsos, Y.C.: Drying in porous media with gravity-stabilized fronts: experimental results. Phys. Rev. E **86**, 026310 (2012b). doi:10.1103/PhysRevE.86.026310

Young, D.M.: Iterative Solution of Large Linear Systems, 1st edn. Academic Press, Orlando, Florida (1971)